Powder Technology 314 (2017) 500–509

Contents lists available at ScienceDirect

Powder Technology

journal homepage: www.elsevier.com/locate/powtec

Experimental and numerical study of particle velocity distribution in the vertical pipe after a 90° elbow

Yong Lu [a,*], Zhenbo Tong [a], Donald H. Glass [b], William J. Easson [b], Mao Ye [c]

[a] Key Laboratory of Energy Thermal Conversion and Control of Ministry of Education, School of Energy and Environment, Southeast University, Nanjing 210096, China
[b] Institute for Materials and Processes, School of Engineering and Electronics, The University of Edinburgh, EH9 3FB Edinburgh, UK
[c] Dalian Institute of Chemical Physics, Chinese Academy of Sciences, Dalian 116023, China

ARTICLE INFO

Article history:
Received 28 July 2016
Received in revised form 3 November 2016
Accepted 29 November 2016
Available online 1 December 2016

Keywords:
Pneumatic conveying
Roping
Particle velocity
Laser Doppler Anemometry

ABSTRACT

A major problem of utilizing co-firing technique is controllably distributing fuel mixtures of pulverized coal and granular biomass in a common pipeline. This research related into particle velocity distribution in the vertical pipe after a right angle elbow was undertaken using the Laser Doppler Anemometry (LDA) technique and a coupled computational fluid dynamics (CFD)-discrete element method (DEM) simulation. According to the similarity criterion of Stokes Number, three types of glass beads were used to model the dilute gas-solid flow of pulverized coal or biomass pellets. In the vertical pipe after an elbow (R/D = 1.3, R is the bend radius as 100 mm and D is pipe diameter as 75 mm), a horseshoe shape feature has been found on cross-sectional distributions of the axial particle velocity for all three types of glass beads on the first section which is 15 mm away from the blend exit. At the further downstream sections, the horseshoe-shaped feature is gradually distorted until it completely disappears. The distance for total disintegration is about 300 mm away from the first section for the first type of glass beads, 150 mm away for the second type and 75 mm away for the third one. As for particle number rate, its cross-sectional distribution on the first section shows that a rope is formed at the pipe outer wall where the maximum particle number rate occurs. On the whole, the rope formed by the first type of glass beads can be still observed at the section which is 450 mm away from the first section. For the second type of glass beads, the rope will disintegrate from the section (300 mm away) according to the cross-sectional distributions of the dimensional value of particle axial velocity divided by air conveying velocity. Overall, the roping characteristic is not obviously shown in the gas-solid flow of the third type of glass beads after the first section. All of these indicate that ropes formed from larger particles disperse more easily, for reasons perhaps related to their higher inertia. In addition, CFD-DEM analysis was employed to determine the particle characteristics to confirm this assumption. The numerical results indicated that the flow pattern has the highest axial velocity near the elbow to form the 'horseshoe' pattern. As the particles with lower Stokes Number were easier to follow the air flow, this is the reason why the horseshoe pattern of smaller particles was more obvious than larger particles.

1. Introduction

In co-firing applications, not only is biomass utilized as a sustainable alternative energy source which saves the usage of fossil fuel, but also CO_2 emission can be reduced through keeping the net amount of CO_2 from the biomass neutral or zero-emission in the atmosphere [1,2]. Co-firing biomass with coal in the same installation has been proved to be an important renewables technology, and it has the great economic advantage of re-using the existing infrastructure of power stations. There has been remarkably rapid progress over the past 5–10 years in the development of the co-utilization of biomass materials in coal-fired boiler plants. Biomass co-firing has been successfully demonstrated in over 228 installations worldwide for most combinations of fuels and boiler types in the range 50–700 MW. Among them, more than a hundred of these were in Europe, and there have been over 40 commercial demonstrations in the United States [3–5].

Before burning in a furnace, the mixed fuel of pulverized coal and biomass should be transported by a kind a pneumatic conveying system which uses air to convey granular materials through a pipeline and has been used commercially to transport the pulverized coal for many years in coal-fired power stations. The current existing pneumatic conveying systems should be retrofitted to be suitable for transporting the fuel blend. These modifications include fuel handling, storage and feed systems [6,7].

Since biomass granules have significantly different characteristics from pulverized coal (for instance, biomass has less heating value than that of coals) and are also more fibrous and less dense, these differences

* Corresponding author.
E-mail address: luyong@seu.edu.cn (Y. Lu).

http://dx.doi.org/10.1016/j.powtec.2016.11.050
0032-5910/

in properties mean that there are potential problems in storage, bulk handling, feeding, combustion, slagging, corrosion and gaseous emissions. According to their air retention properties, Geldart (1973) classified granular materials into four distinct groups A, B, C and D by using density and mean particle size in his fluidization research. The experimental results of Mills [8] confirmed that the materials in group A have very good retention properties and are suitable to be pneumatically transported either in the dense or dilute phase. Biomass density varies from 100 kg/m^3 for straw to 700 kg/m^3 for forest hard wood and coal density ranges from 1100 kg/m^3 for low-rank coal to 2330 kg/m^3 for high density pyrolytic graphite [9]. The pulverized coal used in modern pulverized coal-fired power stations is normally <110 μm in size. However, the granular biomass consumed in many demonstration co-firing power plants is usually filtered to be <3 mm by a 6 mesh sieve before transportation (NETBIOCOF, 2006) [10]. Considering the blockage risk due to transporting oversize granular biomass mixed with pulverized coal in a common pipe, a more suitable granular biomass should be <1 mm in size (equivalent diameter of a sphere) in case of its density around 300 kg/m^3. This kind of granular biomass can be classified in groups A particles and it is suitable for pneumatic conveying according to Mills (2004) investigation.

In research on co-firing applications, most previous studies focused on combustion issues such as combustion efficiency, pollutant formation, carbon conversion, ash management, corrosion, fuel chemistries associated with blending and other downstream impacts. The relevant literature which focuses on transporting the pulverized biomass and coal fuel supply is particularly sparse. Obviously, dilute pneumatic conveying systems are commonly applied to transport pulverized fuel in most coal-fired power plants and there are also numerous experimental and numerical published papers investigating phenomena like gravity setting, roping, erosion, attrition, pressure-wave propagation and gas-solid turbulence modulation etc. in pipes, understanding of the mechanism of pneumatic conveying is still under development due to its complexity. For example, it is still difficult to measure and control the mass flow rate of a solid phase in a pipe and to distribute gas-solid flow from a main pipe to several sub-pipes at an equal mass rate or a specific ratio (DTI, 2003) [11]. The roping phenomenon is also one of great interest in pneumatic conveying research. It occurs in a bend and results in particles being concentrated within a small portion of one pipe cross-section at the bend, as well as in the pipe downstream of the bend, due to particle inertia [12]. Consequently, it is very important to study the Rope disintegration processing after a bend before dual or triple branches are used to deliver particles in a controllable way to the various burners in a pulverized fuel (PF) boiler.

So far, three previous papers which experimentally study particle dynamics in a vertical pipe behind a pipe bend have been searched. Huber and Sommerfeld [13] who used PDA to study the degree of segregation of glass beads with mean size 40 μm under 14 and 21 m/s air conveying velocity with solid loading ratio 0.5 in a vertical pipe behind an elbow. Their experimental data of particle concentration profile displays the rope locating at the region close to the pipe outer wall and the minimum velocity at the pipe outer wall corresponds to the velocity of the dust rope sliding along the wall. They thought it might be caused by momentum losses from particle-wall and inter-particle collisions. Another two experiments [14,15] were done by using a fibre-optic probe to measure time-averaged local particle velocities, concentration and mass fluxes over cross-sections in a vertical pneumatic conveying line following a horizontal-to-vertical elbow under a range of conveying air velocities and solids mass loadings. The profiles of particle concentration show a high particle mass concentration close to the outer wall (along the x negative axis) for four different fluid conditions.

Therefore our research focuses on investigating the characteristics of transporting biomass/coal blends in a vertical pipe downstream of a 90° elbow by using Laser Doppler Anemometry (LDA). Since biomass particle commonly have more irregular shapes, much larger sizes and kinds of density, it is very complicated to define a biomass particle precisely. In order to in order to address the problem of controllable distribution in co-firing techniques and gain an improved understanding of pneumatic conveying mechanisms, three kinds of glass beads were selected to be simulate the dilute gas-solid flow of pulverized coal or biomass pellets according to the criterion of similarity of Stokes Number in our pilot and pioneer experiments.

2. Experimental setup and measurement

In order to characterize the cross-sectional characteristics of the solid phase in different pipe elements of a dilute pneumatic conveying systems, a pilot scale positive pressure dilute pneumatic conveying system was built which involved horizontal and vertical pipes connected by an elbow (R/D = 1.3). The schematic diagram of the experimental apparatus is shown in Fig. 1. The pipe inner diameter and outer diameter are ϕ75 and ϕ85 mm respectively. The effective length of the horizontal glass pipes is 4 m and the vertical is 2 m long. A T piece is used to connect a screw-feeder with the horizontal pipe and several plastic tubes are used to connect a centrifugal fan and a cyclone. This cyclone is used to separate particles from the air at the end of the system. Then particles separated from air are collected in a storage reservoir for recycling in further experiments. Additionally, every metal connector between the pipes is earthed to reduce electrostatic risk due to particle-wall collisions. Air flow is provided by a centrifugal fan with a maximum 0.05 m^3/s volume flowrate under against a 2.2 KPa back-pressure. Air conveying velocity can vary from 10 to 42 m/s by adjusting the pipe back-pressure and the butterfly valve at the inlet of the fan. The maximum particle mass flow rate of the feeder was experimentally determined to be 1.0×10^{-3} kg/s for glass beads with actual density 2550 kg/m^3 and bulk density 1559 kg/m^3.

Since granular biomass is usually lighter and larger than pulverized coal, the question whether they have any similar characteristic in pipe flow is investigated. Stokes Number (St) is defined as the ratio of particle inertia to fluid drag. It is known that a particle having a small Stokes Number has a good capability of following the fluid. We will use the Stokes Number to classify the similarity between pulverized coal and granular biomass characteristics in the direction of fluid flow and apply the terminal velocity (U_{pt}) for the dimensionless analysis of particle velocities in the gravity direction. The detailed equations for calculating the terminal velocity of a particle are listed in the book 'Processing of Particulate Solids' (Seville J.P.K et al., 1997) [16]. Table 1 shows values of St and U_{pt} for typical samples of pulverized coal, wood chips and glass beads.

Experiments were performed under the dilute flow regime with three different sizes of glass beads and smoke. Three types of glass beads were selected to be transported in pipes by air, which were to simulate the dilute gas-solid flow of pulverized coal or biomass pellets [17]. According to the similarity of Stokes Number among particles shown in Table 1, we assumed that the first type of glass beads (<50 μm) and the second (70– 110 μm) should correspond to pulverized coal within 0– 110 μm, as used in power stations. The third group (180– 300 μm) should represent wood-chips around 1 mm equivalent diameter. The data of their mass median particle size are (39, 96, 267) μm respectively according to the data sheet of glass beads provided by the company Worf Glaskugeln GmbH. In addition, smoke was also used to track the air phase of the flow in the LDA experiments.

The instrument of LDA used to measure three dimensional velocity in experiments is a 3D Dantec LDA system [18] which includes two FibreFlow probes with a front lens of f = 800 mm. One probe combines two pairs of beams with wavelengths of 488 nm (blue) and 514.5 nm (green) respectively. The planes produced by the different colored beams are perpendicular to each other. Another probe was integrated with one pair of 476.5 nm beams (violet). As a result, the 3D particle velocity could be measured simultaneously by using these two probes when three pairs of beams focus on the same point. A 40 M shifting Hz frequency of a Bragg cell is selected to determine the particle velocity

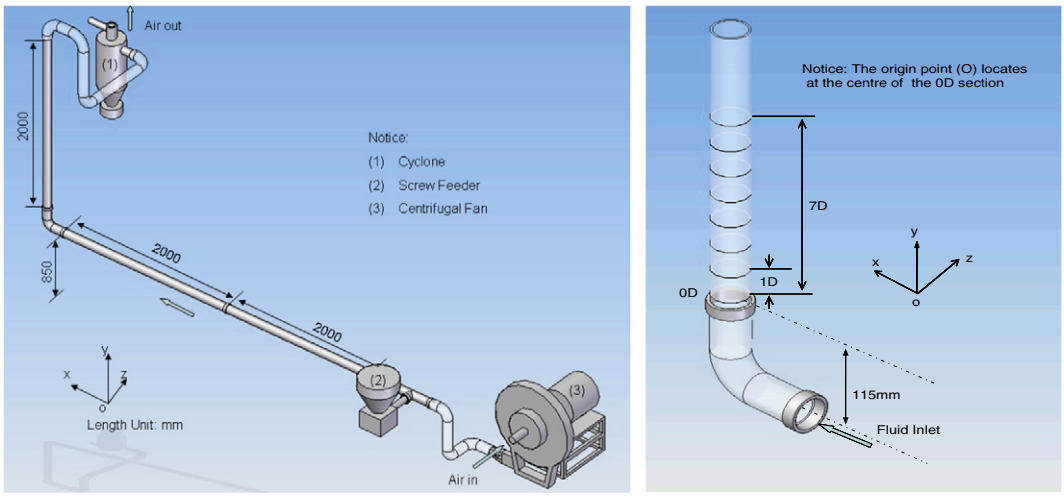

(a) (b)

Fig. 1. (a) sketch of the experimental rig; (b) the arrangement of measurement cross-sections in the vertical pipe.

direction. An extended Laser Doppler Anemometry (LDA) technique [19] has been developed to measure the distributions of particle velocities and particle number over a whole pipe cross section in a dilute pneumatic conveying system. The first extension concentrates on the transform matrix for predicting the laser beams' cross point in a pipe according to the shift coordinate of the 3D computer-controlled traverse system on which the probes of the LDA system were mounted. The second focuses on the proper LDA sample rate for the measurement of gas-solid pipe flow with polydisperse particles. A suitable LDA sample rate should ensure that enough data is recorded in the measurement interval to precisely calculate the particle mean velocity or other statistical values at every sample point. The present study explores the methodology as well as fundamentals of measurements, using a laser facility, of the local instantaneous density of particles as a primary standard.

3. Experimental results and discussion

3.1. Glass beads < 50 μm (the first type)

With regard to the first type of glass beads (<50 μm), the experimental data measured by LDA on the cross-sections from 0D to 6D (here D is the pipe diameter) in the vertical pipe are illustrated in Fig. 2 for the dimensionless axial particle velocity $\{U_{py}/U_a\}$ and the dimensionless horizontal particle velocity $\{U_{px}/\max(\mathrm{abs}(U_{px}))\}$ respectively, under the conditions of an air conveying velocity (U_a) 10 m/s and solid mass loading ratio 0.19% for the first type and 1.9% for the second and third types respectively.

Table 1
Particles Stokes Number and terminal velocity.

Coal(1550 kg/m^3)			Woodchip (185 kg/m^3)	Glass (2500 kg/m3)
d (μm)	Stokes Number	Terminal velocity U_{pt} (m/s)	d (μm)	d (μm)
10	0.072	0.0046	30	8
20	0.287	0.0183	59	16
30	0.645	0.0408	88	24
40	1.147	0.0718	117	32
50	1.793	0.1103	146	40
60	2.581	0.1548	175	48
70	3.514	0.2035	204	56
80	4.589	0.2546	233	63
90	5.808	0.3065	262	71
100	7.171	0.3587	291	79
150	16.13	0.6664	436	119
200	28.68	0.9472	581	158
250	44.82	1.2830	726	197
300	64.53	1.6129	871	237
350	87.84	1.9328	1016	276

In Fig. 2(a), the horseshoe shape can be found on each contour of $\{U_{py}/U_a\}$ from the section 0D to 4D. Generally, the axial particle velocity $\{U_{py}\}$ is faster on the outside portion of the horseshoe (towards pipe outer wall) than that on the inside portion of the horseshoe (towards pipe inner wall). At the further downstream sections of 5D and 6D, the horseshoe-shaped feature no longer exists and the cross-sectional distributions of $\{U_{py}/U_a\}$ have developed into another pattern where a small region with the slower $\{U_{py}\}$ is surrounded a ring with the faster $\{U_{py}\}$. In addition, the region with the slowest $\{U_{py}\}$ on a section is close to the pipe right wall (the z positive direction) behind the section 1D and its area is gradually enlarged from the section 1D to 5D. A similar distribution can be found between the contour of $\{U_{py}/U_a\}$ on the section 5D and that on the section 6D. And the maximum value of $\{U_{py}/U_a\}$ on both sections is decreased as 1 from 1.3 on the section 0D. The similarity suggests that gas-solid flow of the first type of glass beads begin to be steady from the section 5D.

With regard to the dimensionless horizontal particle velocity $\{U_{px}/\max(\mathrm{abs}(U_{px}))\}$ of the first type of glass beads (<50 μm), Fig. 2(b) shows the development of the cross-sectional distribution of $\{U_{px}/\max(\mathrm{abs}(U_{px}))\}$ from the section 0D to 6D in the vertical pipe downstream of a bend. On each section, we assume the pipe inner wall as the start position, where the secondary flow runs towards the pipe outer wall with a decreasing tendency of $\{U_{px}\}$. When the secondary flow reaches at the pipe outer wall, its $\{U_{px}\}$ is close to zero. Then this secondary flow changes its fluid direction from the x positive axis to the x negative axis and it is developed into two sub flows which run towards the pipe inner wall with an acceleration along the pipe left wall and the pipe right wall respectively. As such, the secondary flow forms two sub circulations of one counter-clock wise and one clock wise separately. From the section 0D to 6D, the key difference among secondary flows lies in that the region with the positive maximum $\{U_{px}/\max(\mathrm{abs}(U_{px}))\}$ is gradually shifted from the pipe inner wall to the pipe centre and the total number of isolines is reduced. It is very clear that the secondary flow of the first type of glass beads shown in Fig. 2(b).

3.2. Glass beads within the size range 70– 110 μm (the second type)

Experiments using the second type of glass beads were performed to measure cross-sectional distributions of the axial particle velocity$\{U_{py}\}$

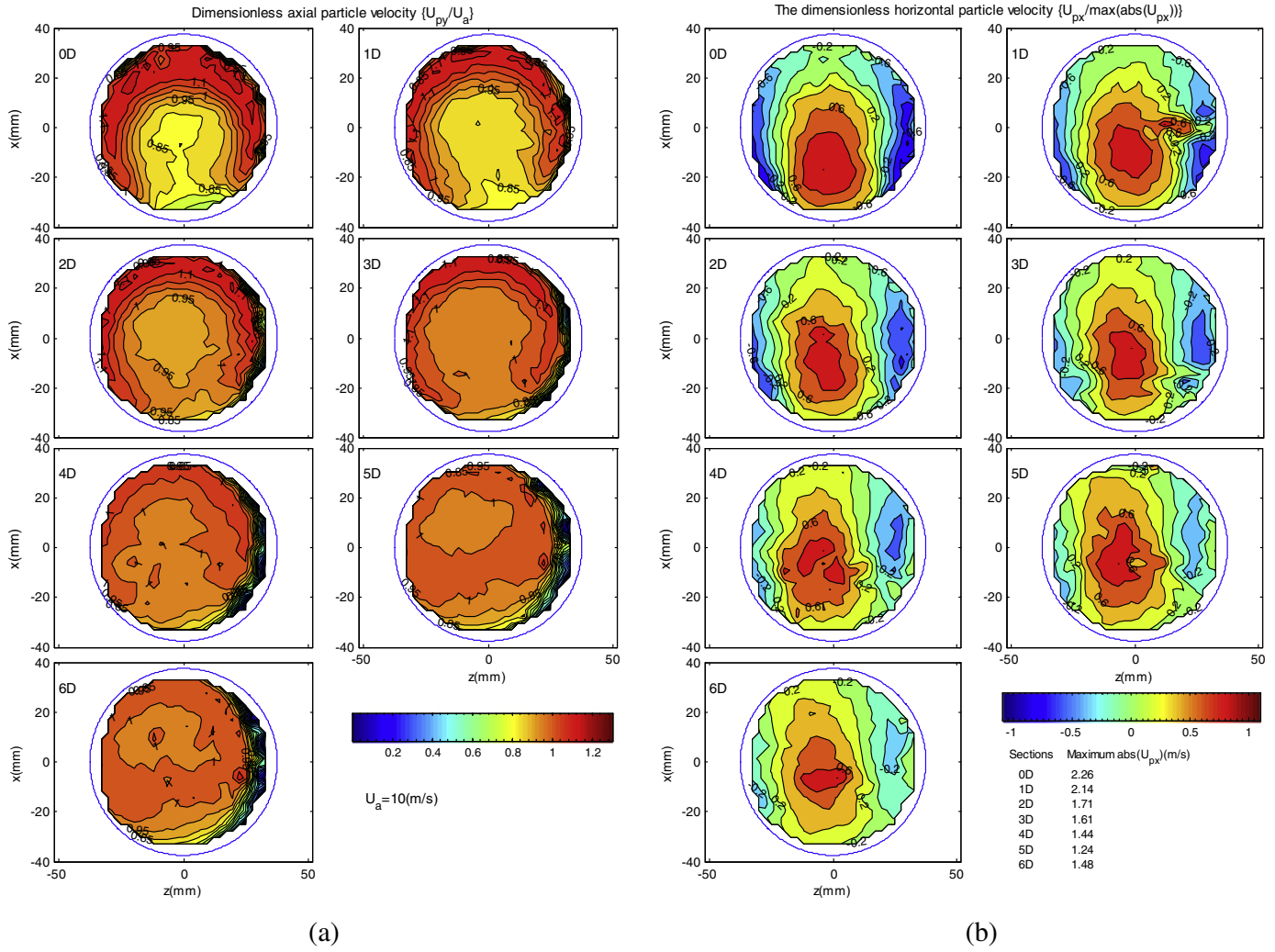

Fig. 2. Development of cross-sectional distributions of (a) the dimensionless axial particle velocity {U_{py}/U_a}; (b) the dimensionless horizontal particle velocity {$U_{px}/\max(\mathrm{abs}(U_{px}))$} of the first type of glass beads (<50 μm).

and the horizontal particle velocity {U_{px}} on the same series of cross-sections as discussed in the proceeding section. Under fluid conditions of air conveying velocity 10 m/s and solid mass loading ratio 1.9%, the experimental data on cross-sectional distributions of three parameters from the sections 0D to 6D are shown in Fig. 3.

As for the dimensionless axial particle velocity {Upy/Ua}, Fig. 3(a) shows the development of its cross-sectional distributions in the vertical pipe downstream of the bend. The horseshoe-shaped feature can be also observed on the contours of {U_{py}/U_a} from the section 0D to 4D, but it is no longer apparent on the contours of {U_{py}/U_a} at the further sections of 5D and 6D. However the contour shape of {U_{py}/U_a} is identical to that on the section 6D, which indicates a steady state of gas-solid flow for the second type of glass beads after the section 5D. All the above observations have a good agreement with those observed in Fig. 2(a) for the first type of glass beads. At a point on each cross-section, the axial particle velocity of the first type in Fig. 2(a) tends to be the corresponding local axial air velocity. But it is less than that of the second type in Fig. 3(a). This phenomenon shows the inertia effect on particle dynamics, since the first type (<50 μm) has a smaller Stokes Number than the second type (70– 110 μm) does. As such, after being accelerated by the fastest air flow, the second type of glass beads would retain its state with a high velocity and the first type tends to follow the current local air flow when both glass beads enter into a region with lower air velocity.

Therefore, the gas-solid flow of the second type of glass beads can be considered as being steady downstream of the section 4D, according to the similarities of cross-sectional distributions of {U_{py}/U_a}.

3.3. Glass beads within the size range 180– 300 μm (the third type)

The experiments were performed using the third type of glass beads within the size range 180– 300 μm, which were transported in the pipe by an air conveying velocity 10 m/s with a solid mass loading ratio 1.9%. The experimental data are plotted in Fig. 4. As for the dimensionless axial particle velocity {U_{py}/U_a}, Fig. 4(a) shows the development of its cross-sectional distributions from the section 0D to 6D in the vertical pipe downstream of the bend. In general, the horseshoe-shaped feature is observed in contours of {U_{py}/U_a} before the section 3D. Further downstream, a clear shape can be no longer observed on contours of {U_{py}/U_a} on the sections of 4D to 6D, where {U_{py}/U_a} is much more randomly distributed and has a larger value > 1 in the main area of a cross-section.

Obviously, the horseshoe-shaped feature is a common characteristic in contours of the axial particle velocity {U_{py}/U_a} in the vertical pipe downstream of a bend for gas-solid flow of three types of glass beads. By contrast, it disappears at the downstream of the section 4D for the first and second types of glass beads and at the downstream of the section 2D for the third one. Therefore, this horseshoe-shaped feature must be formed due to the bend effect which changes a horizontal flow of air

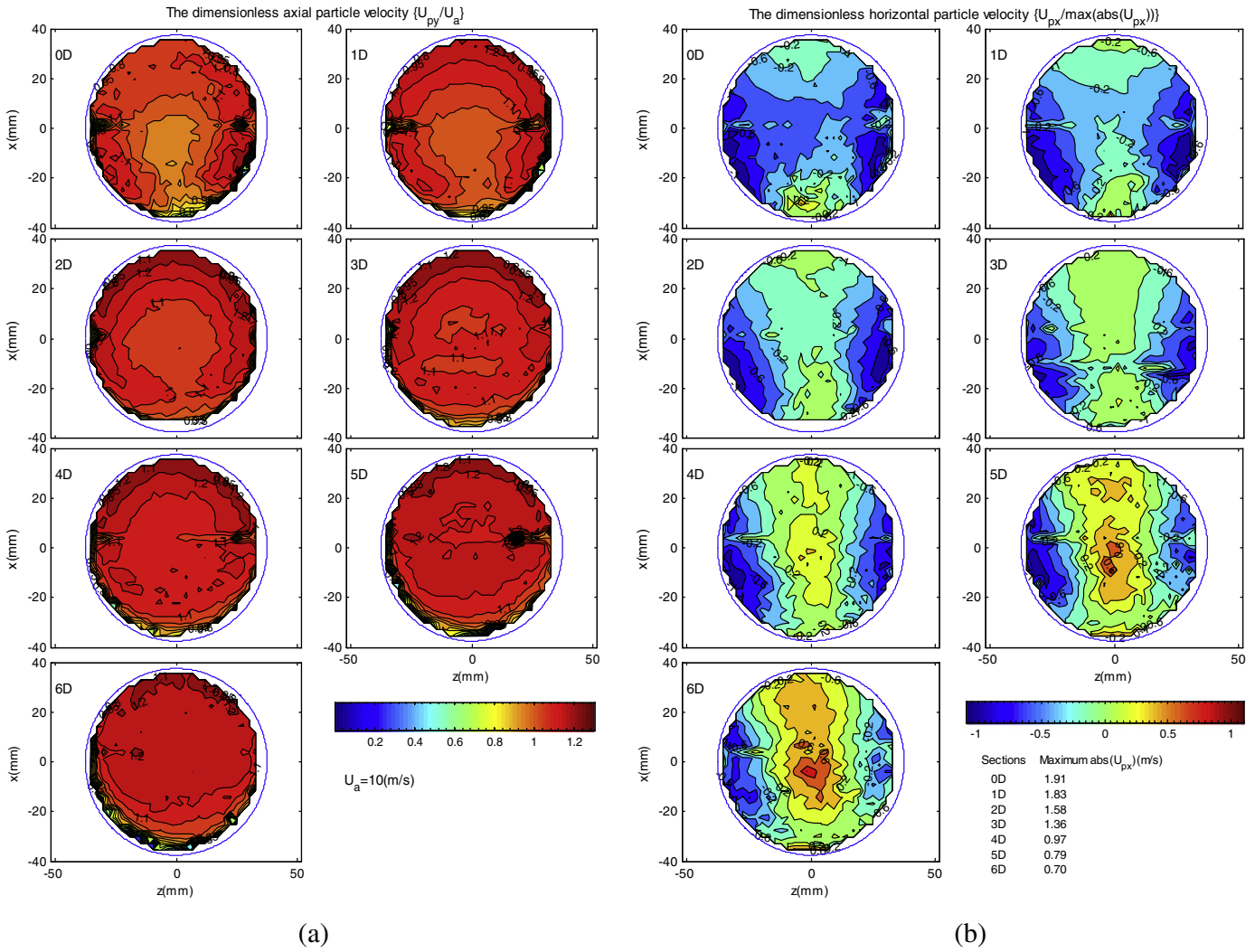

Fig. 3. Development of cross-sectional distributions of (a) the dimensionless axial particle velocity $\{U_{py}/U_a\}$; (b) the dimensionless horizontal particle velocity $\{U_{px}/\max(\mathrm{abs}(U_{px}))\}$ of the second type of glass beads (70– 110 μm).

or gas-solid into the vertical one. The different dispersion positions of the horseshoe indicate that particle Stokes Number plays an important influence on the cross-sectional patterns of $\{U_{py}/U_a\}$ in a vertical pipe behind an elbow. In addition, for the axial particle velocity of three types of glass beads on the main area of the section 6D, it shows that a larger glass bead has a higher axial velocity which is closer to the maximum axial air velocity. This denotes that particle inertia is also one of the most influential factors, for larger glass beads have a stronger ability to keep their previous state of motion.

Contours of the dimensionless horizontal particle velocity $\{U_{px}/\max(\mathrm{abs}(U_{px}))\}$ from the section 0D to 6D are displayed in Fig. 4(b). Unlike those of the other two types of glass beads, each contour of the third type does not show the feature of secondary flow in the vertical pipe downstream of the bend. Overall, there is no clear form shown in contours of $\{U_{px}/\max(\mathrm{abs}(U_{px}))\}$ on the sections of 0D, 1D and 6D. But a similar structure can be seen on the sections from 2D to 4D. Contours of $\{U_{px}/\max(\mathrm{abs}(U_{px}))\}$ on these sections illustrate that a strip in the section middle divides this section into three parts along the x axis. Basically, $\{U_{px}/\max(\mathrm{abs}(U_{px}))\}$ is almost zero in the strip and negative in both sides of the strip. Moreover, the magnitudes of $\{U_{px}/\max(\mathrm{abs}(U_{px}))\}$ have no significant discrepancy on all sections, especially on the section 6D, where $\{U_{px}/\max(\mathrm{abs}(U_{px}))\}$ is almost homogenously distributed with a value of zero over most of the area of the section. Compared with Figs. 2(b) and 3(b), the key difference lies in the lack of structure of secondary flow in Fig. 4(b). This indicates that air secondary flow (the horizontal air velocity) has much more influence on the first and the second types of glass beads than on the third one.

3.4. Particle dynamics in the vertical pipe downstream of a right angle elbow

In order to compare with the previous works, Fig. 5 shows profiles of the axial particle velocity and particle number rate for three type of glass beads along x axis ($z = 0$) from the section 0D of the vertical pipe. The profile data of $\{U_{py}\}$ were extracted from Figs. 2(a), 3(a) and 4(a). Here the x positive axis points to the pipe outer wall. The section 0D is about 15 mm away from the elbow outlet. Compared with contours of $\{U_{py}/U_a\}$ in Fig. 2(a), the $\{U_{py}\}$ profile in Fig. 5 does not illustrate the horseshoe-shaped feature in cross-sectional distribution on the section 0D for all three kinds of glass beads. But the profile of each $\{U_{py}\}$ shows the decreasing tendency from the pipe outer wall to the inner wall (along the x negative axis), which is similar to that observed in the corresponding cross-sectional distributions. In addition, the axial particle velocity of the third type of glass beads is larger than that of the other two types, which indicates the inertial effect on particle velocity, since particles with high inertia should keep their initial velocities rather than easily follow the carrier fluid.

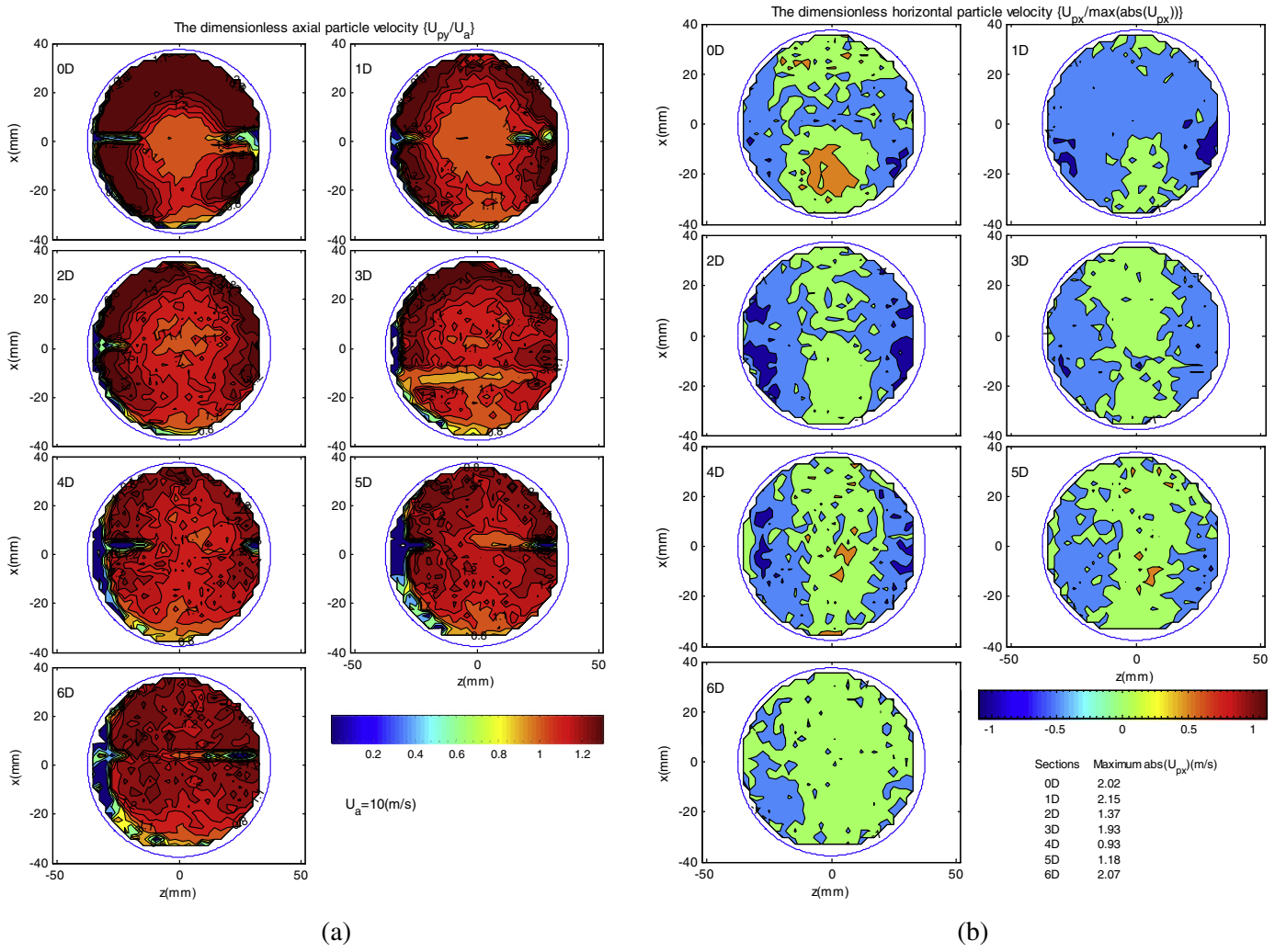

Fig. 4. Development of cross-sectional distributions of (a) the dimensionless axial particle velocity {U_{py}/U_a}; (b) the dimensionless horizontal particle velocity {$U_{px}/\max(\mathrm{abs}(U_{px}))$} of the third type of glass beads (180– 300 μm).

4. CFD-DEM analysis

4.1. Model and simulation condition

In order to discuss the mechanics of particle size effect on solid phase velocity distribution shown in the foregoing experimental results, we also have done some numerical simulations. In a CFD-DEM model, powder dispersion is modelled as a particle-fluid two phase flow in which the behavior of particles is obtained by solving Newton's equation of motion and the continuous air flow is determined by the CFD at the computational cell scale. In the DEM model, the motions of a particle of radius R_i are given by:

$$m_i \frac{\mathrm{d}\mathbf{v}_i}{\mathrm{d}t} = \sum_j \mathbf{f}_{pp,ij} + \mathbf{f}_{pf,i} + m_i \mathbf{g} \tag{1}$$

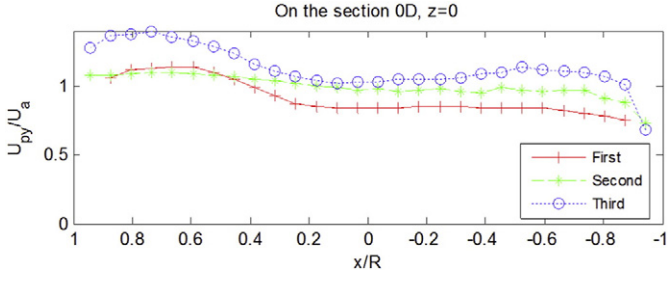

Fig. 5. Profiles of the dimensionless axial particle velocity {U_{py}/U_a} along the x axis on the elbow exit (U_a = 10 m/s, air conveying velocity; Particles: the first type <50 μm, the second type within 70– 110 μm and the third type in 180– 300 μm; R is the pipe radius 37.5 mm).

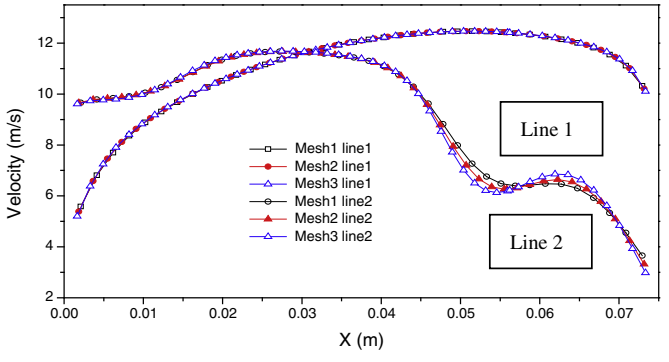

Fig. 6. Comparison of the local velocity profiles produced from the three different meshes (lines 1 and 2 represent two lines near the elbow).

Table 2
Parameters used in the simulations.

Parameter	Value (varying range)
Particle size, D50	39, 97, 110 μm
Particle density, ρ_p	2550 kg m^{-3}
Young's modulus, Y	1×10^8 N m^{-2}
Poisson's ratio,	0.29
Friction coefficient, μ_s	0.3
Rolling friction coefficient, μ_r	0.002
Normal damping coefficient, γ_n	2×10^{-6} s^{-1}
Hamaker constant, H_a	1.2×10^{-19} J
Solid mass loading ratio, λ	0.19%, 1.9%, 1.9%
Gas velocity, v	10 m/s

$$I_i \frac{d\boldsymbol{\omega}_i}{dt} = \sum_j \left(\mathbf{R}_i \times \mathbf{f}_{ct,ij} - \mu_r \left|\mathbf{f}_{cn,ij}\right| \hat{\boldsymbol{\omega}}_i\right) \tag{2}$$

where m_i, I_i, $\mathbf{v}_i$, and $\boldsymbol{\omega}_i$ are, respectively, the mass, moment of inertia, translational and rotational velocities of particle i. $\boldsymbol{f}_{pp,ij}$ is the total force between particle i and particle j or walls, $\mathbf{f}_{pf,i}$ the force between the particle and surrounding fluid. The particle-particle/wall forces $\boldsymbol{f}_{pp}$ include the normal and tangential contact forces $\mathbf{f}_{cn,ij}$ and $\mathbf{f}_{ct,ij}$, the van der Waals force $\mathbf{f}_{v,ij}$. The particle-fluid forces include the drag force, Saffman and Magnus lift forces. Other particle-fluid interactions include the pressure gradient force and Basset force. More detailed discussion of various forces in the DEM-CFD model can be found from [20].

The motion of fluid in CFD model is governed by the Navier-Stokes equations, given by

$$\frac{\partial \varepsilon}{\partial t} + \nabla \cdot (\varepsilon \overline{\mathbf{u}}) = 0 \tag{3}$$

$$\frac{\partial \left(\rho_f \varepsilon \overline{\mathbf{u}}\right)}{\partial t} + \nabla \cdot \left(\rho_f \varepsilon \overline{\mathbf{u}}\overline{\mathbf{u}}\right) = -\nabla P - \mathbf{F}_{fp} + \nabla \cdot (\varepsilon \boldsymbol{\tau}) + \rho_f \varepsilon \mathbf{g} + \nabla \cdot \left(-\rho \overline{\mathbf{u}'\mathbf{u}'}\right) \tag{4}$$

where ε, $\overline{\mathbf{u}}$, $\mathbf{u}'$, ρ_f, P and τ are porosity, fluid mean velocity, turbulent velocity fluctuation, fluid density, pressure and fluid viscous stress tensor, respectively. The volumetric fluid-particle interaction force $\mathbf{F}_{fp}$ is defined as the summation of the particle-fluid interaction $\mathbf{f}_{pf}$ over all the particles in a CFD cell. The CFD-DEM coupling is achieved by exchanging the information obtained from the DEM and the CFD at each step. At every time step with a given fluid flow condition, the DEM determines particle-related information such as the positions, velocities and forces of individual particles. The porosity and volumetric particle-fluid interaction force in the individual computational cells are then calculated and passed to the CFD which uses these data to determine the air flow field and determines the interaction from the fluid to individual particles. The resulting forces are then passed to the DEM to determine the state of particles at the next time step, and the process continues [21].

The dynamics of gas-solid flow in the vertical pipe after 90° elbow was simulated. Mesh independence studies were performed to ensure that the numerical results were independent of the chosen mesh. To obtain mesh independent results, three simulations mesh size of 0.2 mm, 0.4 mm, 0.6 mm corresponding to total nodes 614,790, 793,104 and 1,047,900 was simulated. Velocity magnitude profiles of two lines on the 90° elbow were plotted for the different computational mesh cases (Fig. 6). The line 2 in Fig. 6 shows profiles of the flow velocity along x axis ($z = 0$) from the section 0D of the vertical pipe. Comparing with the Fig. 5, the trend of flow velocity is similar with the particle velocity. The velocity profiles exhibited very small differences on the three computational meshes, indicating mesh independence. The coarsest of the three meshes was used to minimize computational time. A second order bounded differencing was used to resolve all of the flow variables, ensuring minimal numerical diffusion. Turbulence was modelled using the RSM (Reynolds Stress turbulence models). Table 2 lists the parameters used in the simulations.

4.2. Dynamics of air and powder flows

Fig. 7 shows the axial velocity pattern at the steady stage with the air inlet velocity $v = 10$ m/s. It is observed from the side view that the flow has the highest axial velocity near the elbow and from the top view that the 'horseshoe' pattern gradually disappeared along the cross section from 0D to 5D. As the small particle is easier to follow the air flow, this is the reason why the horseshoe pattern of smaller particles' axial velocity is more obvious than larger particles.

The 3D view of the particle volume fraction and particle pattern colored by particle diameter of D50 = 39 μm are illustrated in Fig. 8 As shown on this figure, a particle rope formed after the elbow. This results also confirm that the rope formed by the first type of glass beads can be still observed at the section 6D.

In order to compare with the experimental data, the dimensionless axial particle velocity $\{U_{py}/U_a\}$ and the dimensionless horizontal particle velocity $\{U_{px}/\max(\mathrm{abs}(U_{px}))\}$ regard to the first type of glass beads (<50 μm), from 0D to 6D are illustrated in Fig. 9, respectively. The horseshoe-shaped feature shown in Fig. 9(a) is gradually distorted until it completely disappears from 0D to 6D. And the symmetrical secondary flow pattern is also shown in Fig. 9(b). Both two kinds of the numerical results are consistent with the experimental data in Fig. 3.

As for the larger glass beads, the evolution of their cross-sectional distributions of particle axial velocity and particle horizontal velocity is plotted respectively in Fig. 10 for the second type (70– 110 μm) and

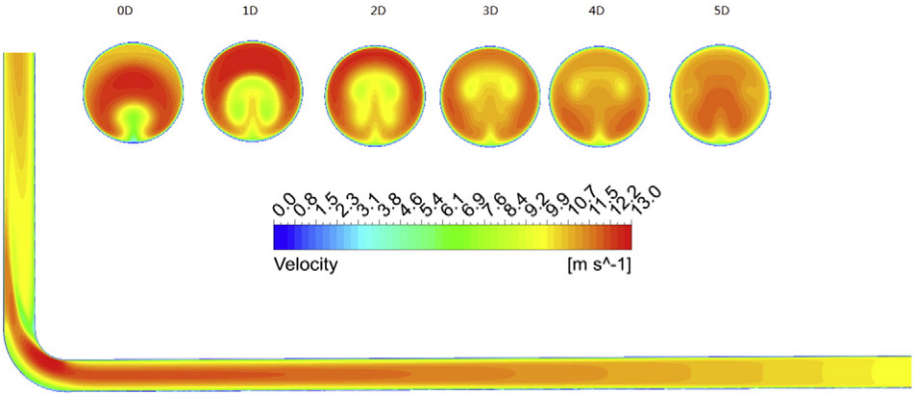

Fig. 7. Side and top views of axial velocity fields (the cross-sections from 0D to 5D).

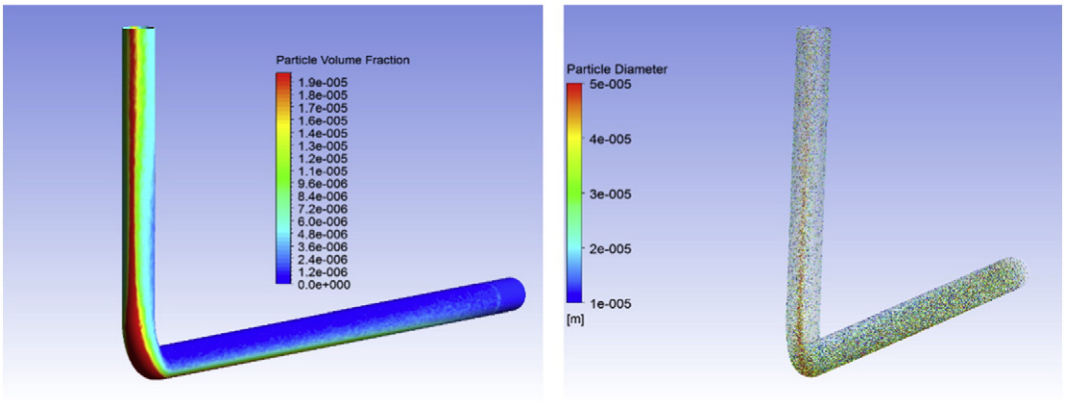

Fig. 8. The particle volume fraction and particle pattern.

in Fig. 11 for the third type (180– 300 μm) under the flow condition of air velocity 10 m/s.

The comparison of the LDA measurements in Fig. 4 with the numerical data in Fig. 10, the horseshoe-shaped feature illustrated by particle axial velocity $\{U_{py}/U_a\}$ is not comparable from the section 0D to 6D. The numerical evolution of particle axial velocity shows that its spatial distribution is nearly homogenous after the section 4D for the second type glass beads and 2D for the third type. However, the numerical development of particle horizontal velocity shows that the secondary flow pattern is clearly kept after the section 2D, which is similar to the experimental data shown in Fig. 4(b).

The evolution of both particle axial velocity and particle horizontal velocity for the third type glass beads is shown in Fig. 11. Similarly, the horseshoe-shaped feature is not clear shown in Fig. 11(a). But the secondary flow pattern is somewhat shown after the section 4D in Fig. 11(b).

To summary the previous discussions, there is a reasonable agreement between the experimental results and the numerical simulations for the small particles of the first type glass beads. As for the larger particles, it is obviously that the experimental phenomena of the horseshoe shaped feature are not clearly predicated by the numerical models.

5. Summary and conclusions

Pneumatic conveying of granular materials is one of the most important applications in many industries. It is essential and necessary to characterize particle dynamics in different components of a pipeline to explore the mechanism of pneumatic transport. In this paper, the

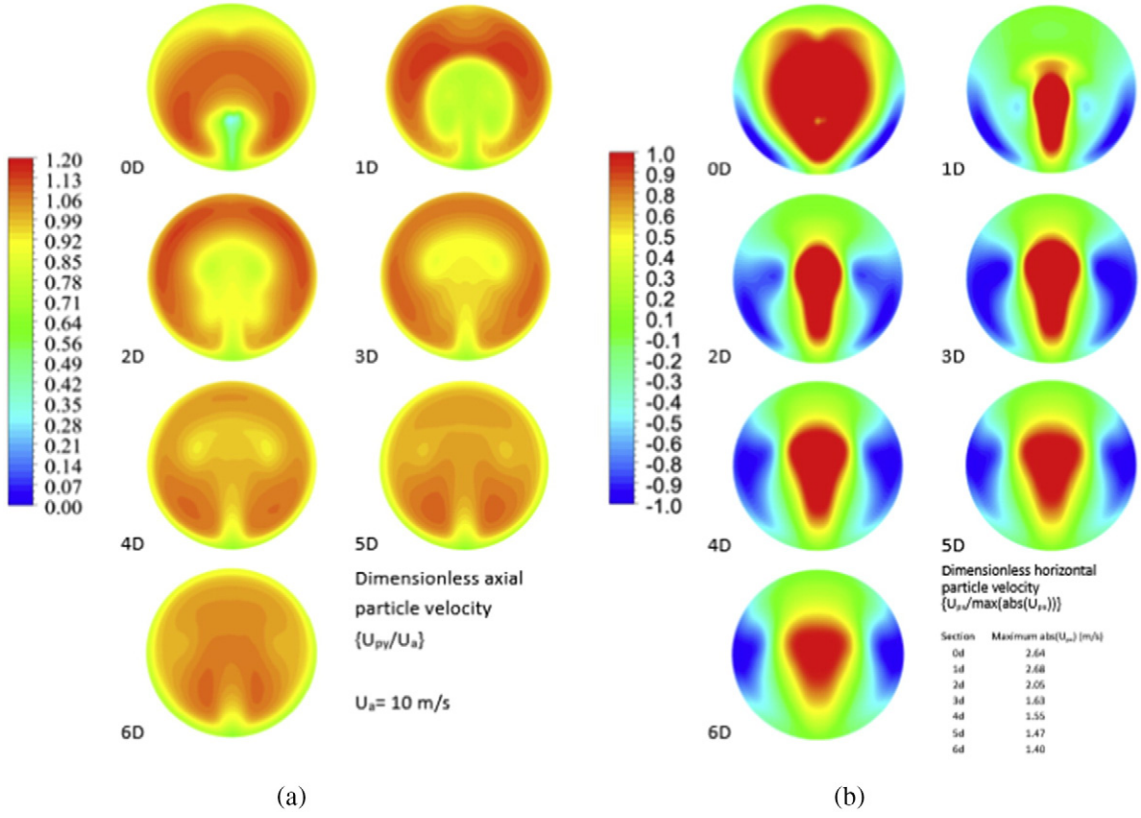

Fig. 9. Numerical results of cross-sectional distributions of (a) the dimensionless axial particle velocity $\{U_{py}/U_a\}$; (b) the dimensionless horizontal particle velocity $\{U_{px}/\max(\mathrm{abs}(U_{px}))\}$ of the first type of glass beads (<50 μm).

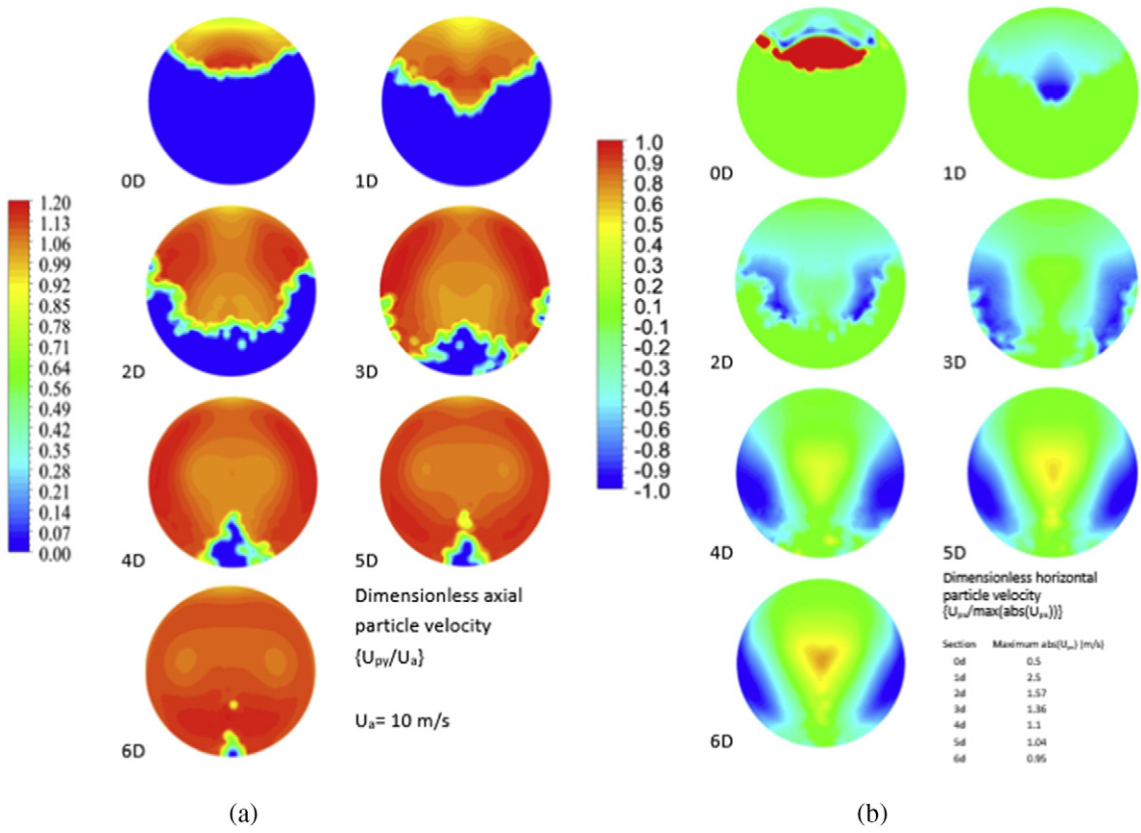

Fig. 10. Numerical results of cross-sectional distributions of (a) the dimensionless axial particle velocity $\{U_{py}/U_a\}$; (b) the dimensionless horizontal particle velocity $\{U_{px}/\max(\mathrm{abs}(U_{px}))\}$ of the second type of glass beads (70– 110 μm).

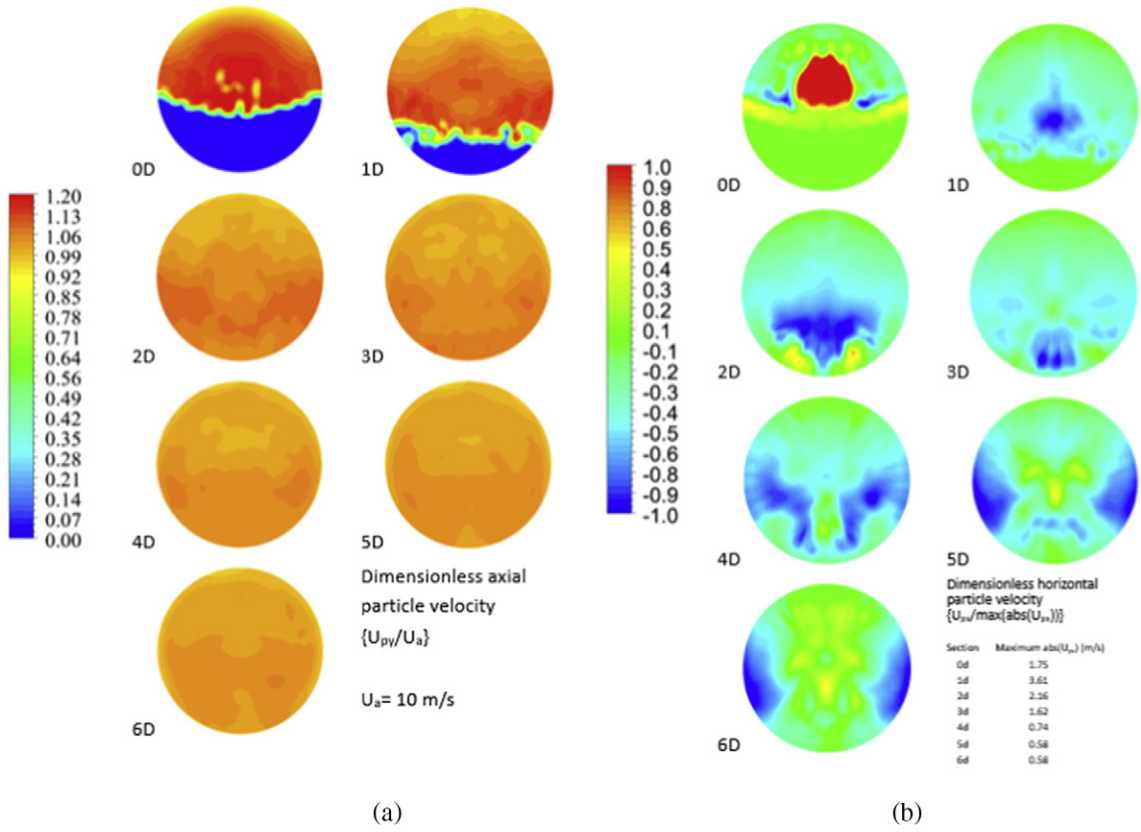

Fig. 11. Numerical results of cross-sectional distributions of (a) the dimensionless axial particle velocity $\{U_{py}/U_a\}$; (b) the dimensionless horizontal particle velocity $\{U_{px}/\max(\mathrm{abs}(U_{px}))\}$ of the third type of glass beads (180– 300 μm).

cross-sectional features of gas-solid flow formed by three types of glass beads in a vertical pipe behind a right angle elbow have been investigated by LDA technique.

In the vertical pipe after an elbow (R/D = 1.3), a horseshoe shape feature has been found on cross-sectional distributions of the axial particle velocity for all three types of glass beads on the section 0D close to the elbow outlet. At the further downstream sections, the horseshoe-shaped feature is gradually distorted until it completely disappears. The distance for total disintegration is about 4D (300 mm away from the elbow exit) for the first type of glass beads, 2D for the second type and 1D for the third one. On the whole, the rope formed by the first type of glass beads can be still observed at the section 6D (450 mm away from the elbow exit). For the second type of glass beads, the rope will disintegrate from the section 4D according to the similarities between cross-sectional distributions of $\{U_{py}/U_a\}$. Overall, the roping characteristic is not obviously shown in the gas-solid flow of the third type of glass beads after the section 0D. All of these indicate that ropes formed from larger particles disperse more easily, for reasons perhaps related to their higher inertia. In addition, CFD-DEM analysis was employed to determine the particle characteristics to confirm this assumption. The numerical results indicated that the flow pattern has the highest axial velocity near the elbow to form the 'horseshoe' pattern. As the particles with lower Stokes Number were easier to follow the air flow, this is the reason why the horseshoe pattern of smaller particles was more obvious than larger particles.

The findings that arise from this project relating to the experimental analysis of particle behavior have explored some fundamental characteristics of particle dynamics in a dilute pneumatic conveying system. Due to the complexity of the phenomena involved, research into gas-solid pipe flow is still an ongoing area of interest, especially for a multiple-component solid phases. In order to obtain empirical equations for particle dynamics in pipe flow, especially in a vertical pipe downstream of a 90° bend, more experimental work using the extended technique of Laser Doppler Anemometry should be carried out to determine the behavior of different granular materials under a wide range of fluid conditions. Our current work only focused on low air conveying velocities.

Acknowledgments

Financial assistance from the National Natural Science Foundation of China (No. 51376048) and the Major Research plan of National Natural Science Foundation of China (Grant No. 91334205) are acknowledged with gratitude.

References

[1] L. Baxter, Biomass-coal co-combustion: opportunity for affordable renewable energy, Fuel 84 (2005) 1295–1302.
[2] AEA, The Sustainability of Biomass in Co-firing (Final Report), 2006 1–4http://www.berr.gov.uk/files/file36485.pdf.
[3] J. Koppejan, Database of biomass co-firing initiatives. IEA, Bioenergy task 32, 2013 http://www.ieabcc.nl/database/cofiring.php.
[4] F. Al-Mansour, J. Zuwala, An evaluation of biomass co-firing in Europe, Biomass Bioenergy 34 (2010) 620–629.
[5] E. Agbor, X. Zhang, A. Kumar, A review of biomass co-firing in North America, Renew. Sust. Energ. Rev. 40 (2014) 930–943.
[6] DTI, in: M. Colechin (Ed.), Best Practice Brochure: Co-firing of Biomass (Report No. COAL R287 DTI/Pub URN 05/1160), E.ON UK, 2007 (http://www.berr.gov.uk/files/file20737.pdf).
[7] W.R. Livingston, Overview of the activities of IEA bioenergy task 32: biomass combustion and co-firing, http://www.berr.gov.uk/files/file39294.pdf2006.
[8] D. Mills, Pneumatic Conveying Design Guide, Elsevier Butterworth-Heinemann, Oxford, UK, 2004 46–47.
[9] D. Ayhan, Combustion characteristics of different biomass fuels, Prog. Energy Combust. Sci. 30 (2014) 219–230.
[10] NETBIOCOF (Integrated European Network for Biomass Co-firing), New and advanced concepts in renewable energy technology biomass, http://netbiocof.net/data/upload/uploads/D14%20STATE%20OF%20THE%20ART%20REPORT%202.pdf2006.
[11] DTI, in: A. Malmgren, G. Oluwande, G. Riley (Eds.), Multiphase Flow in Coal-fired Power Plant (Report No. Coal R252 DTI/Pub URN 03/1635), RWE Innogy plc, 2003 (http://www.berr.gov.uk/files/file20553.pdf).
[12] A. Yilmaz, K.E. Levy, Formation and dispersion of ropes in pneumatic conveying, Powder Technol. 144 (2001) (2001) 168–185.
[13] N. Huber, M. Sommerfeld, Characterization of the cross-sectional particle concentration distribution in a pneumatic conveying system, Powder Technol. 79 (1994) (1991–210).
[14] M. Hussainov, A. Kartushinsky, U. Rudi, I. Shcheglov, G. Kohnen, Experimental investigation of turbulence modulation by solid particles in a grid-generated vertical flow, Int. J. Heat Fluid Flow 21 (2000) 265–373.
[15] P. Dhodapkar, G. Solt, Klinzing, Understanding bends in pneumatic conveying systems, Chem. Eng. 116 (2009) 53–60.
[16] Worf Glaskugeln GmbH, Precision glass beads, http://www.worf.de2008.
[17] Y. Lu, An Investigation of the Particle Dynamics of a Multi-component Solid Phase in a Dilute Phase Pneumatic Conveying System [D], The University of Edinburgh, Edinburgh, 2009 23–25.
[18] DANTEC, Integrated solutions in laser Doppler anemometry, http://www.dantecdynamics.com/Default.aspx?ID=6532008.
[19] Y. Lu, H.D. Glass, J.W. Easson, An investigation of particle behavior in gas-solid horizontal pipe flow by an extended LDA technique, Fuel 88 (2009) (2520–253).
[20] H.P. Zhu, Z.Y. Zhou, R.Y. Yang, A.B. Yu, Discrete particle simulation of particulate systems: theoretical developments, Chem. Eng. Sci. 62 (2007) 3378–3396.
[21] K.W. Chu, B. Wang, A.B. Yu, A. Vince, CFD-DEM modelling of multiphase flow in dense medium cyclones, Powder Technol. 193 (2009) 235–247.